Dalton Transactions

PAPER

View Article Online
View Journal | View Issue

Cite this: *Dalton Trans.*, 2014, **43**, 6536

Electrochemical synthesis, characterization of Ir–Zn containing coordination polymer, and application in oxygen and glucose sensing†

Kum-Yi Cheng,[a] Jing-Chang Wang,[a] Chun-Yen Lin,[a] Wei-Ren Lin,[a] Yi-An Chen,[a] Fu-Ju Tsai,[a] Yu-Chun Chuang,[b] Gu-Ying Lin,[a] Cheng-Wei Ni,[a] Yu-Ting Zeng[a] and Mei-Lin Ho*[a]

Received 13th December 2013,
Accepted 11th February 2014

DOI: 10.1039/c3dt53504e

www.rsc.org/dalton

A simple and sensitive biosensor array based on phosphorescence detection that is able to detect oxygen and glucose in human serum, respectively, has been developed. We demonstrate an electrochemical method as a fast, effective, tunable, and versatile means of growing phosphorescence sensing material. This sensing material, crystalline iridium(III)–Zn(II) coordination polymers, namely **Ir–Zn$_e$**, was grown on a stainless steel mesh and then doped in a sol–gel matrix. The emission of **Ir–Zn$_e$** was ascribed to a metal-to-ligand charge transfer transition (MLCT). The noteworthy oxygen-sensing properties of **Ir–Zn$_e$** were also evaluated. The optimal oxygen-sensing conditions of **Ir–Zn$_e$** with a deduced K_{SV} value of 3.55 were 5 V and 30 °C for 1 hour. Moreover, the short response time (23 s) and the recovery time (21 s) toward oxygen have been measured. The reversibility experiment was carried out for eleven cycles. The resulting >70% recovery of intensity for **Ir–Zn$_e$** on each cycle demonstrated a high degree of reproducibility during the sensing process. The detection limit could be 0.050% for gaseous oxygen. The sensing substrate was subsequently built up under glucose oxidase encapsulated in hydrogel and then immobilized on an egg membrane by the layer-by-layer method. Once the glucose solution was injected into this array, oxygen content depleted simultaneously with a concomitant increase in the phosphorescence of coordination polymers. The linear dynamic range for the determination of glucose was 0.1–6.0 mM, the correlation coefficient (R^2) was 0.9940 (y = 0.75 [glucose] + 0.539), and the response time was less than 120 s. The minimum detectable concentration for glucose was calculated to be 0.05 mM from three times signal to noise. The photophysical properties of the sensing material and the effects of buffer concentration, pH, interference, matrix effect, temperature, and the stability of the biosensor array have also been studied in detail. The biosensor array was successfully applied to the determination of glucose in human serum.

Introduction

There has been intensive research on synthesizing different coordination polymers or metal–organic frameworks (MOFs) for applications such as gas storage, energy storage, catalysis, and optical devices.[1] Among the relevant synthetic methods, electrochemical synthesis offers several advantages for preparing coordination polymers. First, this method allows a continuous production process to produce a higher product content, increasing the profitability and attractiveness for industry. Second, it allows the reaction mixtures under milder reaction conditions, and less reaction time is required than in typical solvothermal or microwave synthesis. Third, it allows greater control and reproducible synthesis related to the particle size.[2a]

Recently, Joaristi *et al.*[2a] used an electrochemical method to synthesize some archetypical MOFs, for which the synthesized samples exhibited suppressed framework flexibility as compared to the compounds obtained by solvothermal methods. Li *et al.* have also employed this method to induce selective deposition of crystalline MOFs.[2b] In another approach, Ameloot *et al.*[2c] demonstrated an electrochemical procedure for growing uniform MOF thin film as a water vapor sensor; the water absorption capacity of the film agreed with values reported in the literature. Although some work has been

[a]*Department of Chemistry, Soochow University, Taipei 111, Taiwan.*
E-mail: meilin_ho@scu.edu.tw; Fax: +886 (2) 2881 1053;
Tel: +886 (2) 2881 9471, ext. 6827
[b]*National Synchrotron Radiation Research Center, Hsinchu, Taiwan*

† Electronic supplementary information (ESI) available: The FT-IR spectra, *in situ* PXRD spectra, absorption and emission spectra, optical and SEM images of **Ir–Zn$_e$** and **Ir–Zn**, interference on the **Ir–Zn$_e$–E–A array**. See DOI: 10.1039/c3dt53504e

focused on developing MOFs by electrochemical synthesis,[2d] to our knowledge, there have been relatively few reports on the respective luminescent MOFs produced electrochemically.

Among the various luminescence materials, phosphorescent iridium complexes are widely used in organic light-emitting diodes. This is due to the photophysical characteristics, which can be readily tuned by changes of the cyclometalating and/or ancillary ligands, thus making such complexes ideal candidates for applications in full color displays.[3] Due to the presence of a heavy metal in MOFs, particularly those containing the iridium atom, the large spin–orbit interaction facilitates an intersystem crossing process that mixes the excited singlet and triplet states. This reduces the lifetime of the triplet state, so phosphorescence is readily observed.[4] Moreover, phosphorescent materials exhibit a conspicuous feature of oxygen quenching, which allows the development of oxygen sensors for biological, industrial, and basic materials science research.

In particular, fast quantitative determination of glucose is important in biology, clinical chemistry, and food analysis.[5] Due to the increase in diabetes worldwide, the development of glucose sensing continues.[6] Several related recognition molecules for glucose attached to fluorophores based on fluorescence enhancement have been investigated including concanavalin A,[7a,b,d] boronic acid derivatives,[7c] glucokinase/hexokinase[7d] and bacterial glucose/galactose-binding protein.[7e] Among the various methods, phosphorescence sensing offers a promising approach for simple and rapid tracking of glucose, without interference from the autofluorescence of a biological system. Furthermore, an effective combination of glucose oxidase (GOx) enables specific glucose sensing and non-invasive glucose monitoring. The detection principle of these optical glucose sensors works on the increase in emission intensity due to the decrease in oxygen level in the oxidation reaction of glucose by GOx; also see eqn (1).[8]

$$\beta\text{-}D\text{-glucose} + O_2 + H_2O \xrightarrow{GOx} \text{D-gluconic acid} + H_2O_2 \quad (1)$$

In our previous study,[9] we reported on the self-assembly of zinc(II) by using $Ir(ppy)_2(H_2dcbpy)PF_6$ (**L-H$_2$**, ppy = 2-phenylpyridine, H_2dcbpy = 4,4′-dicarboxy-2,2′-bipyridine) as the bridging ligand to form crystalline iridium(III)–zinc(II) heterobimetallic containing coordination polymers (**Ir–Zn**) for sensing oxygen. As solved by the oxygen-sensing property analyses, the Stern–Volmer quenching constant (K_{SV}) of **Ir–Zn** is competitive with or even larger than those of many known Ir-complexes. Moreover, in comparison to that of **L–H$_2$** as well as to other coordination polymers, **Ir–Zn** has higher emission intensity and shorter response and recovery times toward oxygen.

Although the above **Ir–Zn** has good sensitivity for oxygen recognition, it is not suitable for further practical pursuit. The main disadvantage lies in the size of crystals, which is difficult to control. Thus, as part of our continuing efforts, we have made further progress in developing a method of electrochemical synthesis capable of providing compelling sensitivity for oxygen recognition. Furthermore, we have created a glitter sensor for glucose recognition (see Fig. 1 and 2).

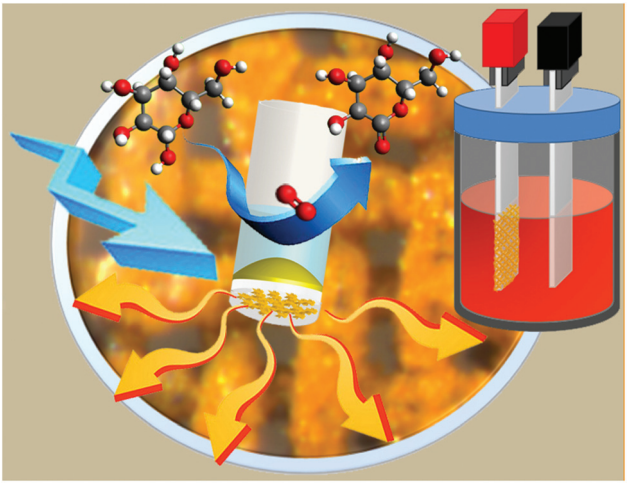

Fig. 1 The schematic illustration of the **Ir–Zn$_e$–E–A array** for glucose sensing.

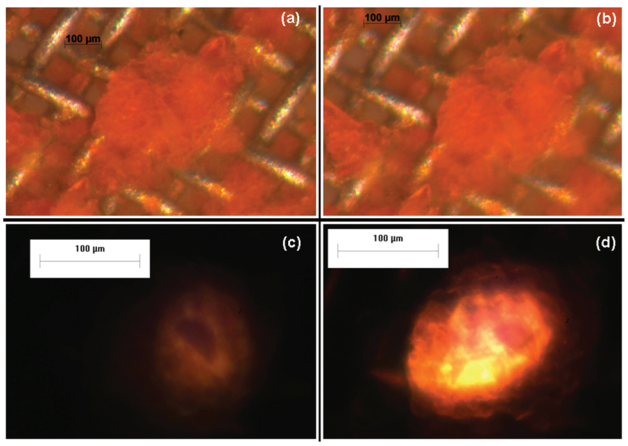

Fig. 2 Color appearance ((a) and (b)) and luminescence changes ((c) and (d)) of representative **Ir–Zn$_e$–E–A array** upon addition of 5 mM glucose (before addition, (a) and (c); after addition, (b) and (d)). Scale bar is 100 μm. λ_{ex} = 405 nm.

Bearing all of this in mind, in this contribution, we demonstrate an electrochemical method as an effective means of growing iridium(III)–Zn(II) containing coordination polymers, $[ZnL_2]\cdot 3DMF\cdot 5H_2O$ (**Ir–Zn$_e$**), for sensing oxygen. The influences of voltage, electrolytic time, and temperature on the resulting structures as well as the photoluminescence properties, oxygen-sensing performance, stability, and other factors are discussed. Subsequently, we report the fabrication of a photoluminescence sensor for glucose by using the layer-by-layer structure as the detection substrate (Fig. 1). First, a sol–gel matrix was used as solid support for the immobilization of compound **Ir–Zn$_e$** as the first layer (**Ir–Zn$_e$ layer**), and fresh eggshell membrane was overlaid as the second layer (**Ir–Zn$_e$–E layer**). The second layer was demonstrated to retain the activity of GOx and to act as a buffer layer. Next, GOx was packaged

into a calcium alginate hydrogel sphere as the third layer (**Ir–Zn$_e$–E–A layer**), resulting in a sensitive glucose sensor system. Based on this sandwiched structure, a detection array (the **Ir–Zn$_e$–E–A array**) has been fabricated, and this array has been coupled with fiber-optic detection for glucose. The influences of the salt effect, pH, temperature, selectivity, stability, and other factors are also discussed. Finally, the proposed method was successfully applied to detect glucose in human serum.

Results and discussion

Electrochemical synthesis and characterization of Ir–Zn$_e$

In an attempt to develop a new strategy and method for fabricating coordination polymer in oxygen and glucose detection, electrochemical synthesis for the production of thin film of **Ir–Zn$_e$** on a stainless steel mesh was performed in the mixed solvents of DMF and water (80 : 25, v/v). This process is driven by the application of the voltage to the zinc electrode, whereupon metal ion Zn^{2+} enters the solution to react with the ligand **L-H$_2$** to afford compound **Ir–Zn$_e$** (see Fig. 1 and Fig. 3(a)). Methyltributylammonium methyl sulfate (MTBS) was used as the additive to increase the conductivity for electrolysis.[10]

For example, after electrolysis for 1 hour at an applied voltage of 20 V and temperature of 10 °C, infrared (IR) spectra, scanning electron microscopy/energy dispersive X-ray spectroscopy (SEM-EDX), powder X-ray diffraction analysis (PXRD), absorption, and emission spectra were collected. The vibration peaks (Fig. S1 in the ESI†) of **Ir–Zn** were in good agreement with that of **Ir–Zn$_e$**, indicating that **Ir–Zn$_e$** and **Ir–Zn** have the same structural motif. The chemical composition of **Ir–Zn$_e$**, characterized by SEM-EDX and EDX mapping, revealed that the elemental constituents were C, O, Zn and Ir (see Fig. 3(b)). The components of Fe and Cr were the signal of the stainless steel mesh. In addition to the SEM and EDX imaging, the obtained thin film of **Ir–Zn$_e$** was further characterized with PXRD (see Fig. 3(c)) and compared to the **Ir–Zn** obtained by the self-assembly method.[9] The measured XRD pattern of **Ir–Zn$_e$** was in good agreement with the pattern of **Ir–Zn**, indicating that the electrolytic material consisted of a phase-pure, single crystal and that the crystal packing of **Ir–Zn$_e$** was the same as that of **Ir–Zn**.

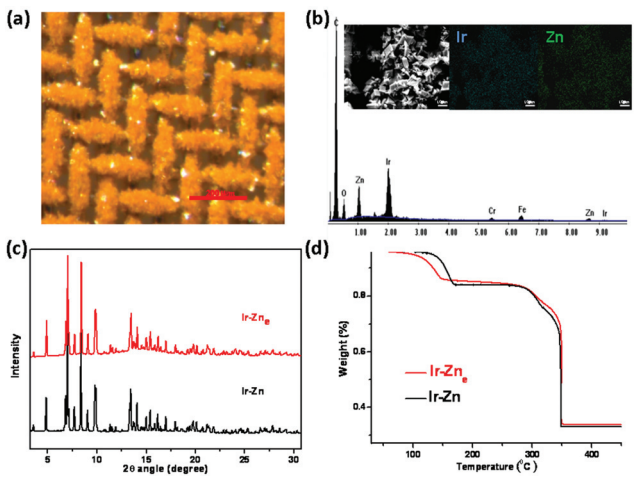

Fig. 3 (a) The optical image of **Ir–Zn$_e$**. Scale bar is 200 μm. (b) The SEM-EDX spectrum of **Ir–Zn$_e$** electrochemically grown on a zinc anode at an applied voltage at 20 V and temperature of 10 °C for 1 h. Inset: (left) SEM images of **Ir–Zn$_e$**; (middle, right) EDX mapping of Ir and Zn elements, respectively. Scale bar = 10 μm. (c) Powder X-ray diffraction patterns of **Ir–Zn** and **Ir–Zn$_e$**. (d) TGA curves for **Ir–Zn** and **Ir–Zn$_e$**.

Thermogravimetric and *in situ* powder X-ray diffraction analysis

The thermal stability of compounds **Ir–Zn** and **Ir–Zn$_e$** were carried out by thermogravimetric analysis (TGA) and *in situ* powder X-ray diffraction analysis. During the heating process, **Ir–Zn** underwent two major weight loss stages, as depicted in Fig. 3(d), with a weight loss in the temperature range from 30 to 170 °C corresponding to the loss of DMF and water molecules (observed, 16.0%; calculated, 16.6%). Further weight loss was observed at 348 °C; the final products were probably Ir_2O_3 and ZnO (observed, 27.1%; calculated, 27.6%). The TG analysis of **Ir–Zn$_e$** also underwent two major weight loss steps in the temperature range of 30–150 °C, which could correspond to the loss of the total 3 DMF and 5 water molecules per formula. On further heating, similar to **Ir–Zn**, **Ir–Zn$_e$** decomposed at ~350 °C.

To further investigate the thermal stability of the materials, *in situ* synchrotron powder X-ray patterns were collected continuously from 25 to 650 °C, and the results at some specific temperatures are shown in Fig. S2(a) and S2(b).† Comparisons of changes of PXRD patterns upon heating between **Ir–Zn$_e$** and **Ir–Zn** are displayed in Fig. S2(a) and S2(b).† The trends are similar. The *in situ* powder X-ray measurements indicated that **Ir–Zn$_e$** converted to a new crystalline form at ~210 °C, completed at ~360 °C. On the other hand, **Ir–Zn** maintained its crystal form from room temperature to 240 °C and the main framework fully decomposed at >360 °C. Therefore, **Ir–Zn** has a higher thermal stability than **Ir–Zn$_e$**; this difference in thermal stability between **Ir–Zn$_e$** and **Ir–Zn** may be attributed to smaller average size of **Ir–Zn$_e$** than that of **Ir–Zn**; *i.e.*, micrometers *versus* millimeters.

The photophysical and oxygen sensing properties of Ir–Zn$_e$

Prior to the discussion of the response behavior of **Ir–Zn$_e$** for oxygen and glucose sensing, the photophysical properties of **Ir–Zn$_e$** under electrolytic conditions at 20 V and 10 °C for 1 h were determined first. The solid state absorption and emission spectra of **Ir–Zn$_e$** and **Ir–Zn** were investigated at RT and are shown in Fig. S3.† The emission of **Ir–Zn**, with a peak wavelength at 613 nm, was attributed to the phosphorescence from the ^{3}MLCT state (Ir → bpy) and has also been reported in our previous work.[9] The absorption and emission bands of **Ir–Zn$_e$** were also broad and structureless, characteristic of the MLCT state. Pertinent data are summarized in Table 1. In comparison to the **Ir–Zn**, the absorption onset of **Ir–Zn$_e$** was blue-shifted relative to that of **Ir–Zn**. Upon 405 nm excitation, the emission spectra for **Ir–Zn$_e$** exhibited a broad emission band centered at 596 nm, which was slightly blue-shifted. This

Table 1 Photophysical properties and oxygen-quenching fitting parameters of **Ir–Zn$_e$** and **Ir–Zn**

	λ_{max} [a]	Q.Y.[a]	K_{SV}	R^2	95% Response time (s)	95% Recovery time (s)
Ir–Zn$_e$	596	0.05	3.55	0.9932	23	21
Ir–Zn	613	0.27	0.834	0.9995	120	110

[a] The emission and quantum yield were detected in crystal at 298 K upon excitation at 405 nm.

suggested that **Ir–Zn$_e$** exhibited a smaller crystal size, or less crystal packing, such that it had less intermolecular interaction to stabilize the whole structure and hence increased the emission energy.[11] This was in agreement with the result of TG analysis (*vide supra*).

The absolute emission quantum yields for **Ir–Zn$_e$** and **Ir–Zn** (see Table 1) were measured to be 0.05 and 0.27, in which **Ir–Zn** was larger than that of **Ir–Zn$_e$** by more than ~5.5 fold. The enhancement in luminescence for **Ir–Zn** (*cf.* **Ir–Zn$_e$**) could be attributed to the greater number of intermolecular interactions, the result of which increased the conformational rigidity of the whole structure,[12] hence reducing the non-radioactive deactivation pathways. Although the quantum yield for **Ir–Zn$_e$** was not larger than that of **Ir–Zn**, the magnitude was still greater than that of relevant iridium complexes (~0.02) and should be more suitable for oxygen- and glucose-sensing applications (*vide infra*).[13]

As displayed in the inset of Fig. 4(a) and (b), **Ir–Zn$_e$** with the maximum K_{SV} value was obtained at an applied voltage of 5 V and temperature of 30 °C for 1 h, so these settings were selected for further analysis of the oxygen-sensing properties (*vide infra*). After exposure to different oxygen concentrations of O_2 at room temperature, phosphorescence intensities decreased (Fig. 4). Subsequently, the kinetics of a photophysical intermolecular deactivation process between the compound **Ir–Zn$_e$** and oxygen was determined by the Stern–Volmer plot. Accordingly, the peak intensity of emission was plotted against the mole fraction of O_2 in nitrogen (see inset of Fig. 4 (c)). The quenching constant between **Ir–Zn$_e$** and oxygen can thus be deduced from the Stern–Volmer equation[13] *via* the relationship of the ratio between emission intensity, I_0/I, *versus* partial pressure of O_2 (P_{O_2}) expressed in eqn (2),

$$\frac{I_0}{I} = 1 + K_{SV}P_{O_2} \quad (2)$$

where I_0 denotes the total emission in the absence of oxygen and K_{SV} is the associated Stern–Volmer quenching constant. Accordingly, the K_{SV} value of **Ir–Zn$_e$** can be deduced from the value of the slope to be 3.55 (R^2 = 0.9932). The error bar represents the standard deviation (N = 3). The K_{SV} value is larger than the result of **Ir–Zn** (K_{SV} value = 0.834, R^2 = 0.9995) reported previously.[9] The above result showed that compound **Ir–Zn$_e$** has a higher sensitivity toward oxygen than **Ir–Zn** does. This result can be rationalized by the fact that the crystal size of **Ir–Zn$_e$** is smaller than that of **Ir–Zn** and hence results in higher surface area to collide with oxygen.

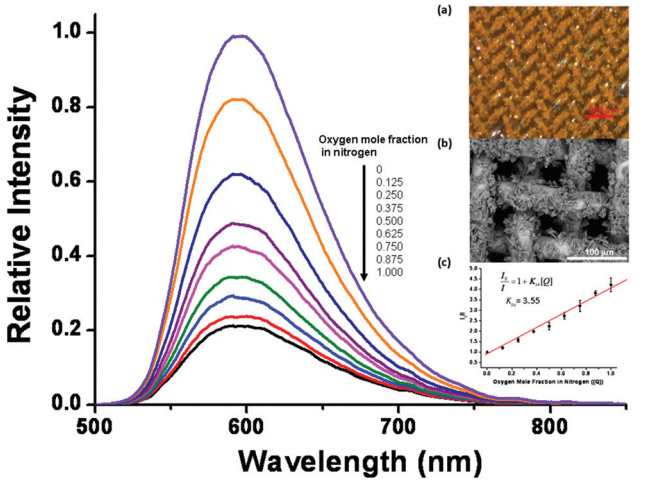

Fig. 4 Response of **Ir–Zn$_e$** under different mole fractions of O_2(g) in nitrogen. λ_{ex} = 405 nm. Inset: (a, b) the optical image of **Ir–Zn$_e$** and the SEM image of **Ir–Zn$_e$** electrochemically grown on a zinc anode at an applied voltage of 5 V and temperature of 30 °C for 1 h. Scale bars are 200 μm for (a) and 100 μm for (b), respectively. (c) Stern–Volmer plot for the oxygen quenching of **Ir–Zn$_e$**. The solid lines are the best fitting line using eqn (2) (see text). The error bar represents the standard deviation (N = 3).

Influence of electrolytic time on the formation of Ir–Zn$_e$ and corresponding oxygen sensing properties of Ir–Zn$_e$

To assess the influence of electrolytic time on the formation of **Ir–Zn$_e$**, the morphologies and corresponding oxygen sensing properties of **Ir–Zn$_e$** were measured. The optical images, SEM images, average sizes, and corresponding average K_{SV} values are presented in Table 2. Average K_{SV} values were obtained from at least three measurements. At a voltage of 20 V and temperature of 40 °C, electrolytic time increased from 2 min, to 10 min, 30 min, 1 h, 2 h, and 3 h, respectively. The sizes of **Ir–Zn$_e$** on the mesh increased with time and the K_{SV} values increased with the change in time from 2 min to 1 h and then decreased at longer times. The changes in size could be attributed to the enhanced release of Zn^{2+} by an increase in the electrolytic time. When the electrolytic time was prolonged to 4 h (data are not shown here), the amount and the size of **Ir–Zn$_e$** on the mesh started to decrease, and crystals started to precipitate on the bottom of the vessel, indicating that the **Ir–Zn$_e$** crystals were too big to deposit on the mesh.

The average K_{SV} values of **Ir–Zn$_e$** increased to about 0.93 when the electrolytic time was increased to 1 h and started to decrease after 1 h. This was probably because the amount of **Ir–Zn$_e$** and the size at 1 h were larger and more homogeneous than other conditions. The optimal electrolytic time for the following experiment was selected to be 1 h. As compared with the **Ir–Zn** produced by the self-assembly method, the formation time of **Ir–Zn$_e$** by the electrochemical method was significantly decreased and still possessed a promising high K_{SV} value.

Table 2 Influence of electrolytic time on the formation of **Ir–Zn$_e$**, corresponding optical images, SEM images, and oxygen-sensing properties

Electrolytic time	2 min, 40 °C, 20 V	10 min, 40 °C, 20 V	30 min, 40 °C, 20 V
Optical image	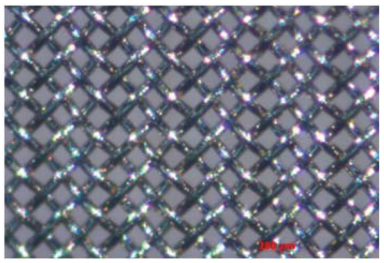	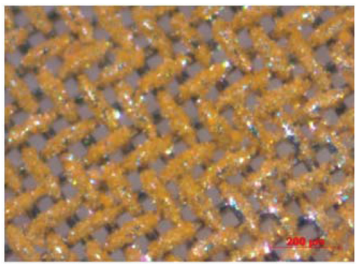	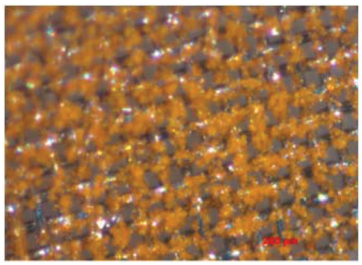
SEM image	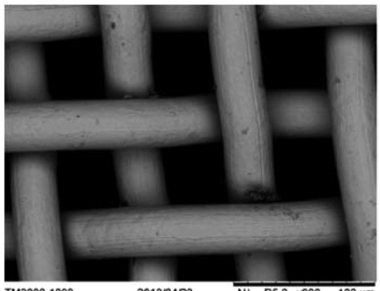	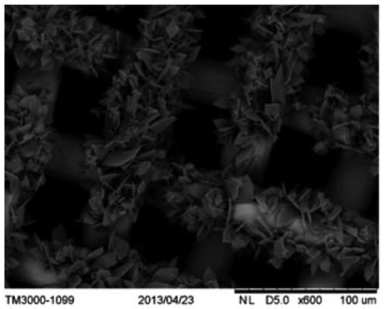	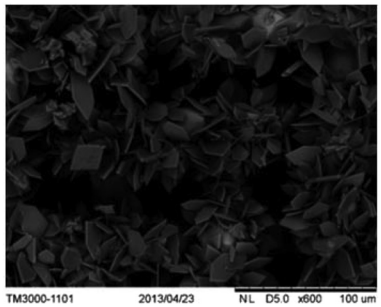
K_{SV}[a]/*average size*[b] (*μm*)	0.05/1.90	0.72/12.3	0.79/15.2

Electrolytic time	1 h, 40 °C, 20 V	2 h, 40 °C, 20 V	3 h, 40 °C, 20 V
Optical image	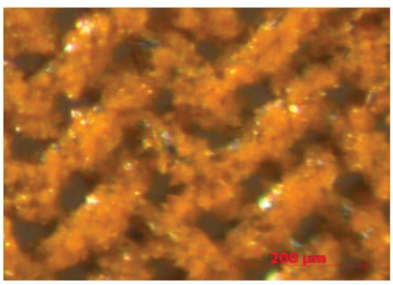	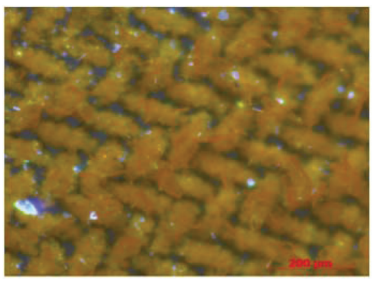	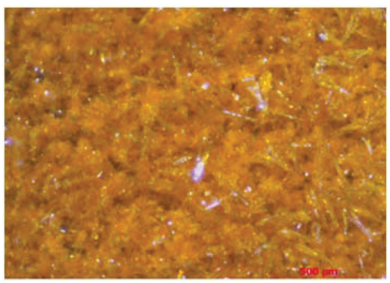
SEM image	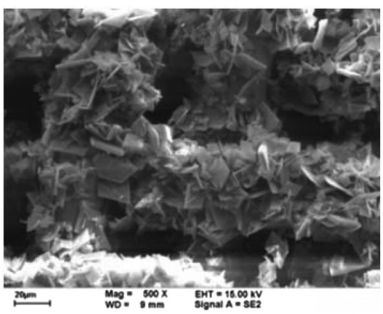	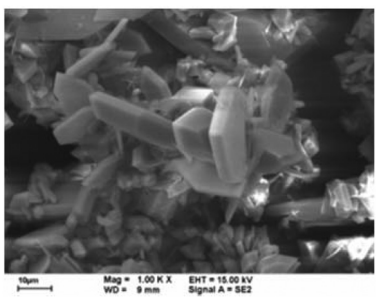	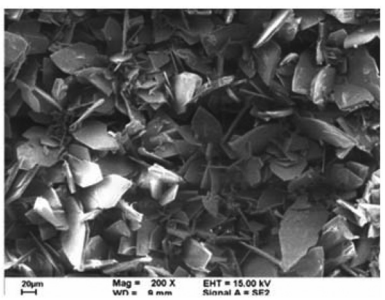
K_{SV}/*average size* (*μm*)	0.93/17.9	0.85/78.1	0.80/93.4

[a] K_{SV} values were obtained from at least three measurements. [b] The **Ir–Zn$_e$** sizes were measured diagonally and were constructed on the basis of three SEM photographs, with at least 300 crystals for each condition.

Influence of electrolytic temperature on the formation of Ir–Zn_e and corresponding oxygen sensing properties of Ir–Zn_e

Table S1 in the ESI† illustrates the morphologies and oxygen-sensing properties of **Ir–Zn_e** when synthesis temperature was increased. At an elevated temperature (up to 40 °C), the elevated solubility of the ligand **L–H_2** allowed the sizes of electrochemically grown **Ir–Zn_e** to increase. At higher temperature, similar to the reason mentioned before, the crystals sizes on the mesh started to decrease. Also, the rate of crystal growth increased upon increasing the reaction temperature; some of the crystals formed in the reaction vessel and not on the mesh, and hence decreased the yield of **Ir–Zn_e** on the mesh. The best K_{SV} value toward oxygen is depicted in Table S1† at 30 °C.

Influence of electrolytic voltage on the formation of Ir–Zn_e and related oxygen sensing properties of Ir–Zn_e

To increase the applied voltage between the electrodes, *i.e.*, to increase the electrostatic forces, the electrolytic voltage was increased from 5 V to 30 V. The details are presented in the Experimental section. Table S2† showed the optical images, SEM images, average sizes, and corresponding average K_{SV} values. These results confirmed that increasing the voltage increased the size of **Ir–Zn_e**. These results also indicated that the optimal oxygen-sensing condition was at 5 V and 30 °C for 1 h. Among all conditions, we found that **Ir–Zn_e** was smallest at 5 V, while the number of crystals was the largest and the homogeneity was the best. Therefore, to obtain a larger K_{SV} value, the factors of homogeneity and amount of product are more important than the size.

Sensitivity, the response and the recovery performances, recycle test of Ir–Zn_e as an oxygen sensor

The sensitivity of **Ir–Zn_e** along with the response and recovery performances represents two major characteristics of the sensor. To examine the sensitivity of the sensor, as shown by the ratio of I_0/I at the mole fraction of 0.125 (see Fig. 4), the quenching of luminescence for **Ir–Zn_e** produced at 5 V and 30 °C for 1 h could reach 1.22. This experiment confirmed the noteworthy sensitivity of **Ir–Zn_e** for oxygen. Also, the limit of detection of **Ir–Zn_e** for gaseous oxygen was calculated to be 0.05% from three times signal to noise. As previously reported, an equivalent dissolved oxygen concentration of 9.2 ppm for air saturated water[14] was taken into consideration; this optical sensor was able to achieve detection limits up to 5.0 ppb.

The observed 95% average response time was 23 s by the decrement of emission intensity by 95% after exposure of 100% N_2 to 100% O_2 (Fig. S4†). The 95% observed average recovery time was reduced to 21 s by the increase of emission intensity to 95% after exposing 100% O_2 to 100% N_2. The related response times and recovery times of **Ir–Zn_e** are presented in Table 1. The above results showed that the detection limit and reaction kinetics toward oxygen of **Ir–Zn_e** were greater than those of **Ir–Zn** by more than ten and six fold, respectively. This result can be rationalized by the fact that the crystal size of **Ir–Zn_e** is smaller than that of **Ir–Zn**, and hence results in higher surface area to collide with oxygen (*vide supra*).

As shown in Fig. S4,† the experiments for **Ir–Zn_e** were carried out for eleven repeated cycles, and luminescence intensities were recorded after each step. As a result, the >70% recovery of intensity for **Ir–Zn_e** on each cycle demonstrated the high degree of reproducibility during the sensing process. Taking advantage of a large K_{SV} value, compound **Ir–Zn_e** obtained at 5 V and 30 °C for 1 h was employed as a paradigm for the following glucose-sensing experiments.

Response behavior of the Ir–Zn_e–E–A array for glucose

As shown in Fig. 5(a), upon the addition of glucose under 405 nm excitation, an increased emission of the **Ir–Zn_e–E–A array** maximized at 596 nm was observed, indicating that oxygen consumption in the reaction reduced the quenching of the phosphorescence of **Ir–Zn_e** and resulted in a leap in emission intensity. Owing to the similarity in spectral features, the emission can unambiguously be assigned to a ^{3}MLCT emission. Therefore, this is the manner in which **Ir–Zn_e** is used as a reporter moiety in our design of a glucose sensing system (*vide supra*). Furthermore, upon the addition of glucose to the **Ir–Zn_e–E–A array**, under similar 405 nm excitation, an increased emission still maximized at 596 nm was observed. This also indicated that there was no interference from cross-layer interactions.

Fig. 5(b) displays the relative emission responses of the **Ir–Zn_e–E–A array** to different concentrations of glucose while maintaining a constant glucose oxidase concentration and temperature of 25 °C. Upon exposure to glucose, the relative emission change against the reaction time in Fig. 5(b) was curvilinear, eventually leveling off to a constant value. As

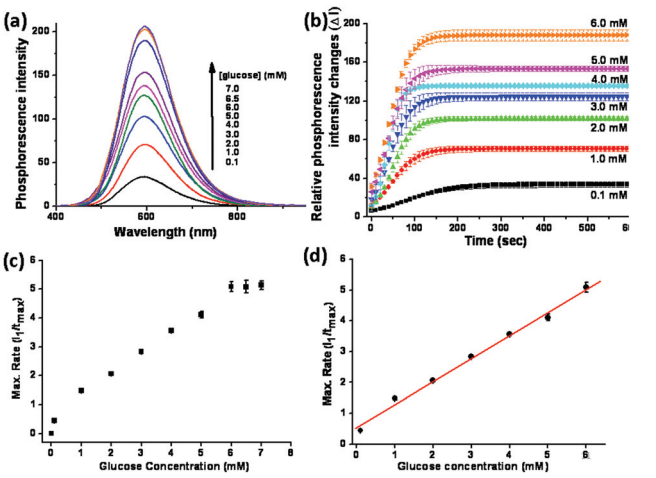

Fig. 5 (a) The emission spectra of the **Ir–Zn_e–E–A array** upon exposure to different concentrations of glucose. (b) The kinetic responses of the **Ir–Zn_e–E–A array** upon addition of different concentrations of glucose (N = 3). (c) Calibration plot of the **Ir–Zn_e–E–A array** at various glucose concentrations. (d) The linear calibration curve in the range of 0.1–6.0 mM glucose. Error bars are calculated from three replicate measurements (N = 3).

expected, the emission changes increased as glucose concentration increased. The error bar represents the standard deviation (N = 3). As shown in Fig. 5(b), the emission response increased sharply, accompanied by decreases in reaction time with increasing glucose concentrations, because abundant free GOx was available to bind the added glucose.[15] Also, the result showed that enzymatic activity was retained with this sensing architecture.

In order to analyze the enzyme kinetic behavior from the above results, the dynamic transient method[16] was selected, and the response curve was fitted by eqn (3) in the Experimental section.

$$I_t = I_1 + \frac{I_0 - I_1}{1 + e^{(t - t_{max})dt}} \quad (3)$$

Accordingly, the maximum changing rate of phosphorescence intensity (I_1/t_{max}) under different glucose concentrations was thus deduced from the plot, and a calibration curve (0.0 mM–7.0 mM) was established (see the Experimental section and Fig. 5(c)). Fig. 5(d) shows that the linear calibration curve with the correlation coefficient (R^2) was 0.9940 (y = 0.75 [glucose] + 0.539) in the concentration range of 0.1 mM to 6.0 mM. As shown in Fig. 5(b), the limit of detection was the lowest quantity of glucose added into the **Ir–Zn$_e$–E–A array** that could be distinguished from the absence of that glucose. The minimum detectable concentration (LOD) for glucose was calculated to be 0.05 mM from three times signal to noise. This array offers a good glucose-detection capability (0.05 mM–6.00 mM) as compared to commercially available phosphorescence probes.[17]

Moreover, it should be noted that for the **Ir–Zn$_e$–E–A array**, the detection time (<120 s) was more promising than previously reported.[8,17,18] To support this contention, the linear response range and response time of various glucose biosensors based on the use of GOx are listed in Table 3. These results demonstrate the validity of the electrochemical procedure for growing a uniform and small MOF for the enhancement of the glucose-sensing capability.

Effect of buffer concentration

Phosphate buffer was used in this study not only to maintain the proper environment within GOx with the advantage of transparency in the UV region but also to stabilize the pH of the solution, thus keeping the enzyme activity at its maximum.[25] We next investigated the effect of buffer concentration on the maximum changing rate of phosphorescence intensity with 5 mM glucose (Fig. 6(a)). The rate increased with the elevation of buffer concentration and reached its maximum at 100 mM, which can be attributed to the conformation changes of the enzyme making oxygen more accessible.[15] A decrease in the buffer concentration above 100 mM was probably due to the inhibition of the enzyme activity in the high ionic strengths.[26]

Effect of pH

The activity of an enzyme is affected by its environmental conditions. The optimum pH of a solution was subsequently

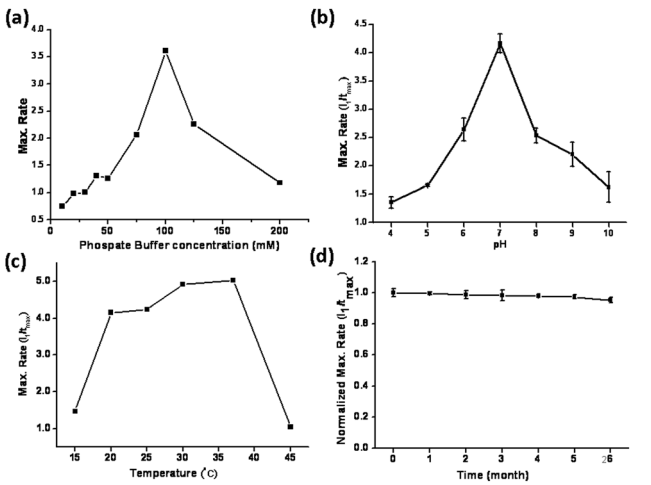

Fig. 6 Effect of buffer concentration (a), pH (b), temperature (c) and stability test (d) on the maximum response rate of the **Ir–Zn$_e$–E–A array** upon exposure to 5 mM glucose. (b, d) Each datum was obtained from an average value of three replicate measurements (N = 3).

Table 3 Comparison of the performances of the various types of optical glucose biosensors based on the use of GOx

Luminescence materials	Linear response range	LOD	Response time	References
Ru-dpp derivative[a]	0.0–0.6 mM	58 μM	5 min	Yang *et al.* (2006)[8]
Ru-dpp derivative[b]	0.10–5.0 mM	0.06 mM	6 min	Chang *et al.* (2010)[17]
PVA-Py[c]	0.25–3.0 mM	0. 19 mM	?[d]	Odaci *et al.* (2009)[19]
Ru-dpp derivative[a]	0.10–0.80 mM (20 °C)	?[d]	5 min	Zhou *et al.* (2005)[20]
Ru-dpp complex[e]	9.0–200 μM	9.0 μM	6–9 min	Wu *et al.* (2004)[21a,b]
Ru-dpp complex[f]	0.0–0.50; 0.5–3.0 mM	3.6 μM	6 s	Wang *et al.* (2008)[18,22]
Ru-dpp complex[f]	0.1–5.0 mM	?[d]	6 min	Endo *et al.* (2006)[22,23]
Ru(phen)$_3$[g]	1.0–20.0 mM	?[d]	2 min	Rossi *et al.* (2004)[24]
Ir–Zn MOFs[h]	0.05–5.0 mM	0.01 mM	<240 s	Our previous results[9]
Ir–Zn$_e$	0.1–6.0 mM	0.05 mM	<120 s	This work

[a] Tris(4,7-diphenyl-1,10-phenanthroline)ruthenium(II) ditetrakis(4-chlorophenyl)borate. [b] Tris(4,7-diphenyl-1,10-phenanthroline) ruthenium dichloride. [c] Poly(vinyl alcohol)-pyrene. [d] Not mentioned in the article. [e] Tris(4,7-diphenyl-1,10-phenanthroline) ruthenium(II) didodecyl sulfate. [f] Tri(4,7-diphenyl-1,10-phenanthroline) ruthenium(II) perchlorate. [g] Dichlorotris(1,10-phenanthroline) ruthenium(II) hydrate. [h] Ir(ppy)$_2$(H$_2$dcbpy)PF$_6$.

Table 4 Detection of glucose in human serum

	Concentration (mM)					
Human serum	Claimed value	Proposed method[a]	Glucose added (mM)	Glucose found[a] (mM)	Recovery (%)	R.S.D.[b] (%)
Concentration 1	1.836 ± 0.027[c]	1.8356 ± 0.0028				0.15
2			0.25	0.2537 ± 0.0021	101.47	0.84
3			0.50	0.5026 ± 0.0037	100.53	0.73
4			0.75	0.7528 ± 0.0142	100.37	1.89
5			1.00	0.9986 ± 0.0106	99.86	1.06
6	4.194 ± 0.059[c]	4.1963 ± 0.0039				0.09
7			0.25	0.2538 ± 0.0059	101.53	2.31
8			0.50	0.4659 ± 0.0052	99.61	1.06
9			0.75	0.7686 ± 0.0170	102.48	0.87
10			1.00	1.0027 ± 0.0012	100.27	0.12

[a] Average of three determinations. [b] R.S.D.: relative standard deviation. [c] The glucose concentrations in human serum were certified by the definitive method, isotope dilution gas chromatography mass-spectrometry.[30]

evaluated. Fig. 6(b) shows the effect of solution pH on the maximum response rate of the **Ir–Zn$_e$–E–A array** upon exposure to 5 mM glucose. The optimal pH value is usually reported as 8 for free GOx.[27] In our case, the results clearly indicated that the optimum response rate of phosphorescence intensity occurred at pH 7.0 for the **Ir–Zn$_e$–E–A array**. Accordingly, the buffer solution of pH 7.0 was used in further testing and clinical analysis.

Effect of temperature

It is known that enzyme activity and reaction kinetics are also affected by temperature. Fig. 6(c) illustrates the effect of reaction temperature on the maximum changing rate of phosphorescence intensity of the **Ir–Zn$_e$–E–A array** with 5 mM glucose at pH 7.0. As seen in that figure, the maximum changing rate increased with temperatures up to 30–37 °C and decreased afterwards. At lower temperature (<40 °C), increasing the temperature will increase the frequency of collisions, thereby increasing the reaction rate. At elevated temperature (>40 °C), emission is very rapidly thermally quenched, hence decreasing the reaction rate.[28] In order to operate conveniently and prolong the lifetime of the GOx, room temperature (25 °C) was chosen as the working temperature for all experiments.

Effect of interferents

The effects of lactose, D-galactose, sucrose, D-fructose, maltose monohydrate, citric acid, succinic acid, uric acid, tartaric acid, ascorbic acid, and urea (10 mM) on the phosphorescence responses of the **Ir–Zn$_e$–E–A array** were studied. As shown by the response rate equivalent to glucose after adding potential interferents (Table S3†), none of the possible interferents presented any significant interference to the response of the **Ir–Zn$_e$–E–A array**. Thus, this experiment confirms the noteworthy selectivity of the **Ir–Zn$_e$–E–A array** for glucose.

Stability of the Ir–Zn$_e$–E–A array

This work investigated the six-month stability of the **Ir–Zn$_e$–E–A array** with glucose 5 mM by measuring the response rate. The **Ir–Zn$_e$–E–A array** was stored at 4 °C and then allowed to stand at room temperature until thawed prior to use. From stability of the **Ir–Zn$_e$**, aging and degradation of the egg membrane or Octyl-triEOS/TEOS, a systematic study on degradation mechanisms for the **Ir–Zn$_e$–E–A array** aged for six months was conducted. The results (Fig. 6(d)) showed that the maximum response rate was repeatable, and the values of around 95% of its initial value demonstrated the high degree of reproducibility and stability. The error bar represents the standard deviation (N = 3). Also, according to a previous report,[29] a slight deterioration of transition–metal complexes, *e.g.* **Ir–Zn$_e$**, decreased the light absorption efficiency of **Ir–Zn$_e$** and subsequently decreased the response rate.

Sample analysis

Finally, the **Ir–Zn$_e$–E–A array** was applied to the practical analysis of glucose in an actual serum sample. A commercially available, serum-based standard reference material for glucose (NIST SRM 965) adequately served as a material to be analyzed. The concentrations of glucose in serum were determined by the **Ir–Zn$_e$–E–A array** to be 1.8356 ± 0.0028 and 4.1963 ± 0.0039 mM, respectively (N = 3). This result is in agreement with the concentrations of glucose in serum, 1.836 ± 0.027 and 4.194 ± 0.059 mM (N = 3), respectively, as determined by the definitive method for glucose, isotope dilution gas chromatography mass-spectrometry.[30] As displayed in Table 4, the recovery tests for glucose were performed by adding four known amounts of glucose into the sample solutions, which were then analyzed with the **Ir–Zn$_e$–E–A array**. The recoveries of these measurements ranged from 99.86% to 101.53% for 1.836 ± 0.027 mM glucose, and from 99.61% to 102.48% for 4.194 ± 0.059 mM glucose, respectively. The results demonstrated here show the **Ir–Zn$_e$–E–A array** to be quite suitable for glucose detection in real samples.

Conclusions

Several conclusions can be drawn from this study: (1) a sensing material, **Ir–Zn$_e$**, has been synthesized electrochemically, and a detection array (the **Ir–Zn$_e$–E–A array**) has been

fabricated, coupled with fiber-optic detection for gaseous oxygen and glucose in human serum, respectively. (2) The optimal oxygen-sensing condition of **Ir–Zn$_e$** with a deduced K_{SV} value of 3.55 was at 5 V and 30 °C for 1 hour. For practical applications, the response, recovery, and reversibility of the array have been successfully demonstrated. The observed 95% average response time was 23 s, and the 95% observed average recovery time was 21 s. The reversibility experiment was carried out for eleven repeated cycles. As a result, the >70% recovery of intensity on each cycle demonstrates the high degree of reproducibility during the sensing process. Also, the detection limit could be 0.050% for gaseous oxygen. The results show a promising K_{SV} value, response, and recovery time that are competitive with or even greater than those of many known Ir-complexes. (3) Under the optimum conditions, the linear dynamic range for the determination of glucose was 0.1–6.0 mM with the correlation coefficient (R^2) of 0.9940 (y = 0.75 [glucose] + 0.539), the response time was less than 120 s, and the sample volume was less than 5 μL. The minimum detectable concentration for glucose was calculated to be 0.05 mM from three times signal to noise. The sensing capability and the response time were better than those of many known optical glucose sensors. (4) Electrochemical synthesis offers several advantages, such as continuous production of a uniform and small product (**Ir–Zn$_e$**), a milder reaction condition, less reaction time, and a more controllable and reproducible method of synthesis related to the particle size. (5) Our proposed method to detect oxygen and glucose provides the advantages of simplicity, sensitivity, reproducibility, stability, and low cost. Accordingly, it is clear that a future extension of this method should be versatile and prospective.

Experimental sections

General information and materials

All solvents were obtained from commercial suppliers and were used without further purification unless otherwise noted. The infrared spectrum was measured using a Perkin Elmer 2000 FTIR spectrometer with KBr pellets.

The tetraethyl orthosilicate (TEOS) and triethoxy(octyl)-silane (Octyl-triEOS) were purchased from Sigma-Aldrich. Glucose oxidase (GOx, EC 1.1.3.4 from *Aspergillus Niger*) with a specific activity of 195 700 U g^{-1} of lyophilized solid was purchased from Sigma (Cat no. G2133). Phosphate buffer saline at pH 7.0 was prepared by using 0.1 M Na_2HPO_4 and NaH_2PO_4.

Electrochemical synthesis of [ZnL$_2$]·3DMF·5H$_2$O (Ir–Zn$_e$)

Compound **Ir–Zn$_e$** was synthesized with reference to Ameloot *et al.*[2c] and Cha *et al.*[31] Two zinc electrodes were used in the cell, and a stainless steel mesh was attached to one side of the zinc electrode (anode) (see Fig. 1). Under a nitrogen atmosphere, an aqueous solution of 100 mg of **L-H$_2$** was dissolved in 80 mL of DMF and mixed with 1 g of methyltributylammonium methyl sulfate (MTBS) in 25 mL of H_2O under vigorous stirring for 30 min. Then the voltages, currents, and operating temperatures were applied. After 1–4 hours, an orange-red solid from the solution precipitated on the anode. Finally, the product was collected by filtration, washed with water/ethanol, and dried under nitrogen gas. The morphology was examined by scanning electron microscopy (SEM; LEO 1530 and Hitachi Tabletop TM-3000). Elemental analysis of products was performed by using a Hitachi TM-3000 tabletop electron microscope (EDS, Hitachi Tabletop TM-3000).

Based on the ohmic drop law, the cell voltage required in the electrochemical experiment can be deduced *via* the relationship expressed in eqn (4):

$$\Delta V = I\frac{\ell}{aC} \tag{4}$$

where ΔV is the voltage difference supplied by the energy source, I is the current, ℓ is the distance between the zinc electrodes, a is the cross-sectional area of the electrodes, and C is the conductivity of the solution. In our cell configuration, we have values for three of the four quantities in eqn (4): ℓ = 2.5 cm, a = 3 cm^2, and C has been measured at 0.68 mS cm^{-1} at room temperature. If we send I = 0.02 A through a solution, the expected voltage required in our electrochemical cell can be deduced to be 24.5 V. Accordingly, the voltages applied in this experiment ranged from 5 to 30 V. As an example, after electrolysis for 1 hour at an applied voltage of 20 V and a temperature of 30 °C, IR spectrum of **Ir–Zn$_e$** was collected. IR (KBr) ν (cm^{-1}): 3424 (w), 3053 (w), 1719 (w), 1608 (w), 1582 (w), 1544 (vw), 1479 (w), 1357 (w), 1313 (w), 1267 (w), 1233 (w), 842 (w), 758 (w), 736 (w), 675 (vw), 559 (w).

Thermogravimetric analysis of Ir–Zn and Ir–Zn$_e$

Thermogravimetric analysis (TGA) of **Ir–Zn** and **Ir–Zn$_e$** was performed with a computer controlled TGA Q500 V20.7 instrument (TA Instruments). Samples of **Ir–Zn** and **Ir–Zn$_e$** were loaded into platinum holders and heated with a ramp rate of 3 °C min^{-1} from room temperature to 800 °C in an air flow of 60 mL min^{-1}.

Synchrotron powder X-ray diffraction experiments of Ir–Zn and Ir–Zn$_e$

The powder X-ray diffraction experiments (PXRD) of **Ir–Zn** and **Ir–Zn$_e$** were performed at the beamline BL01C2 at the National Synchrotron Radiation Research Center (NSRRC) in Taiwan. The ring energy and current of the NSRRC were operated at 1.5 GeV and 300 mA in top-up injection mode. The wavelength of the incident X-rays for **Ir–Zn** was 1.0332 Å (12 keV), and that for **Ir–Zn$_e$** was 0.6199 Å (20 keV), respectively, delivered from a 5 Tesla superconducting wavelength shifting magnet and a Si (111) double crystal monochromator. Variable temperature PXRD for **Ir–Zn** and **Ir–Zn$_e$** were carried out from 25 to 650 °C with a heating rate of approximately 10 °C min^{-1}. The powder sample was sealed in a quartz capillary (1.0 mm) and heated with a stream of hot air; each PXRD pattern was exposed for about 3 min. The two-dimensional diffraction pattern was recorded with a Mar345 image plate detector and converted to a one-dimensional XRD profile using the FIT2D program with cake type integration.[32] The sample to detector distances were

341.46 mm for **Ir–Zn** and 401.54 mm for **Ir–Zn$_e$**, respectively, and the diffraction angle was calibrated by the NIST standard reference materials Ag behenate and Si (SRM640c) powders. For easy and intuitive comparison of the PXRD data of **Ir–Zn** and **Ir–Zn$_e$**, the patterns were plotted with photon energy of 12 keV and are shown in Fig. 3(c).

Spectral measurement and gaseous oxygen-sensing of Ir–Zn$_e$

UV-vis diffusive reflectance spectroscopy spectra of **Ir–Zn** and **Ir–Zn$_e$** were obtained with a HITACHI U-3900H spectrophotometer equipped with an integrating sphere accessory (Al_2O_3 was used as a reference).[33] In order to investigate the possible differences in photoluminescence of **Ir–Zn** and **Ir–Zn$_e$** due to the variation of crystal size and crystal growth quality, **Ir–Zn** and **Ir–Zn$_e$** were measured with a confocal mode of a Mono-Vista confocal Raman microscope system (Princeton Instruments/Acton).

The oxygen-sensing properties of **Ir–Zn** and **Ir–Zn$_e$** worked on the principle of luminescence intensity quenching. In this approach, a 406 nm laser line (GaN laser, 406 nm) was used as an excitation source throughout the measurements. A set of neutral density filters was then placed in the beam path to attenuate the laser power. N_2 (99.99%) and O_2 (99.99%) were mixed at different concentrations *via* mass flow controllers and passed into a Linkam THMS 600 hot stage (Linkam Scientific Instruments, United Kingdom) equipped with a video camera (Qimage 5.0 RTV), in which the optics had been specially made to allow both UV (up to 280 nm) excitation and emission. The microscope (Olympus BX51) had an upright-style frame in which all optics were modified to allow the passage of deep UV to infrared light. Simultaneously, a video camera (Qimage 5.0 RTV) was used to capture images. The excitation area is 1 mm^2 diameter circular. The output flow rate of the gas mixture was maintained at 500 mL min^{-1}. The O_2 concentrations were accurate to 0.1%. The photoluminescence was separated from the scattering light of excitation pulse by an edge filter with a cut-off wavelength of 420 nm (3RD420LP, Omega Optical). Subsequently, the luminescence was collected by an optical assembly to the entrance slit of a polychromator (blazed at 500 nm), which was coupled with a sensitive charge coupled detector (CCD, Princeton Instruments, PI-MAX). The CCD was operated in shutter mode, and the measurements were performed with 100 ms exposure time. Quantum yields were measured using an absolute PL quantum yield measurement system (Hamamatsu Photonics C9920-02).

Fabrication of glucose sensing layer (Ir–Zn$_e$ layer)

The glucose sensing **Ir–Zn$_e$ layer** was prepared by a modified sol–gel method, following Chu *et al.*[34] The sensor was fabricated using **Ir–Zn$_e$** on mesh (1.5 mm × 1.5 mm) encapsulated in an Octyl-triEOS/TEOS composite sol. Typically, 0.58 mL TEOS and 1.22 mL Octyl-triEOS were mixed first; then 1.25 mL EtOH and HCl (0.1 M, 0.4 mL) were added to the solution to catalyze the reaction. The resulting mixture was capped and stirred for another 1 h at room temperature. Then 3.5 mL EtOH was added to the mixture and stirred for 1 h to generate a sol solution.

After that, **Ir–Zn$_e$** on mesh (1.5 mm × 1.5 mm) was added into a new micro-centrifuge tube (Labcon, Petaluma, CA, USA) and a sol solution (2 μL) was pipetted into this tube. Finally, this tube was wrapped in aluminum foil and the sample was left to solidify at room temperature for 2 hours, after which the product **Ir–Zn$_e$ layer** was obtained.

Immobilization of GOx encapsulation in calcium alginate on eggshell membrane (Ir–Zn$_e$–E–A layer) and the fabrication of the Ir–Zn$_e$–E–A array

In brief, eggshell membrane was purchased from a local market. The membrane was rinsed with DI water and then cut to a circle 2 mm in diameter. When the **Ir–Zn$_e$ layer** dried, eggshell membrane was overlaid on it (**Ir–Zn$_e$-E layer**) in a micro-centrifuge tube. Separately, 4 wt% sodium alginate (1 mL) aqueous solution was heated to 120 °C for 1 hour in a round-bottomed flask. After cooling to room temperature, the sodium alginate solution was mixed with GOx (5 mg) in 0.1 M phosphate buffer (1 mL). The mixed solution (2 μL) was added to the **Ir–Zn$_e$–E layer**. After this, calcium chloride aqueous solution (200 μL, 0.2 M) was added to the **Ir–Zn$_e$–E layer** slowly to crosslink the alginate in a micro-centrifuge tube and then centrifuged at 10000 rpm for 10 min. Finally, the residue solution was removed by dropper, and the **Ir–Zn$_e$–E–A layer** in a micro-centrifuge tube was generated. The **Ir–Zn$_e$–E–A array** can contain sixteen micro-centrifuge tubes. The **Ir–Zn$_e$–E–A array** was fabricated by inserting the **Ir–Zn$_e$–E–A layer** in the micro-centrifuge tubes to two lines of eight strips (prisma, BP-B69301).

Spectral measurement of glucose sensing

For all of the glucose sensing experiments, the emission spectra and kinetic curves of the **Ir–Zn$_e$–E–A array** upon addition of different concentrations of glucose solution were measured with a bifurcated optical fiber system (QBIF600-UV-VIS, Ocean Optics). In this approach, a 405 nm LED (LLS-405, Ocean Optics) was used as the excitation source throughout the measurement. The photoluminescence was separated from the scattering light of an excitation pulse by an edge filter with a cut-off wavelength of 455 nm (LLS-405, Ocean Optics). When the emission intensity of the **Ir–Zn$_e$–E–A array** in the micro-centrifuge tube reached a steady state, 5 μL of different concentrations of glucose solution were injected into each tube. Subsequently, the luminescence and the kinetic curve were collected by a charge-coupled device area image sensor (QE65000, Ocean Optics) and the associated software from Ocean Optics. The fiber-optic data were collected every 10 s for 10 min.

Analysis of phosphorescence changing rate

The emission changing rate of the **Ir–Zn$_e$–E–A array** can be deduced *via* the relationship of phosphorescence intensity at the time t, I_t, *versus* time (t), expressed in eqn (3),[16b]

$$I_t = I_1 + \frac{I_0 - I_1}{1 + e^{(t - t_{max})dt}} \quad (5)$$

where I_0 and I_1 are the phosphorescence intensities at the beginning and at reaching saturation, respectively. T_{max} denotes the time point of inflection in the curve and is the time point where the maximum rate of phosphorescence intensity increase was observed, and dt is the time range for the most significant phosphorescence changes. First, the kinetic courses of phosphorescence intensity responses of the **Ir–Zn$_e$–E–A array** fit eqn (3). On the other hand, t_{max} can be deduced from a plot of phosphorescence changing rate (dI/dt) *versus* time (t). Finally, the maximum response rate of the array upon exposure to different glucose concentrations can thus be expressed by I_1/t_{max}. As a result, the rate of the phosphorescence changes can be explored.

Analysis of glucose concentration in human serum

Standard Reference Material 965b (SRM 965b), obtained from NIST, is human serum, provided frozen in flame-sealed glass ampoules. Each unit of SRM 965 has four pairs of ampoules, each ampoule containing 2.00 ± 0.04 mL of serum. The serum in each pair of ampoules has one of four glucose concentrations, certified by the definitive method for glucose, isotope dilution gas chromatography mass-spectrometry.[30] The resulting serum solutions were filtered using the Nanosep centrifugal device with a cut-off of 3 kDa (Omega; Pall Corp., East. Hills, NY) at 14 000 rpm and 4 °C for 10 min. The phosphorescence changing rate of the signal of each concentration was measured with the **Ir–Zn$_e$–E–A array**.

Acknowledgements

Generous support from the National Science Council of Taiwan and the Ministry of Education is acknowledged.

References

1 N. Stock and S. Biswas, *Chem. Rev.*, 2012, **112**, 933–969.
2 (*a*) A. M. Joaristi, J. Juan-Alcañiz, P. Serra-Crespo, F. Kapteijn and J. Gascon, *Cryst. Growth Des.*, 2012, **12**, 3489–3498; (*b*) M. Li and M. Dincă, *J. Am. Chem. Soc.*, 2011, **133**, 12926–12929; (*c*) R. Ameloot, L. Stappers, J. Fransaer, L. Alaerts, B. F. Sels and D. E. De Vos, *Chem. Mater.*, 2009, **21**, 2580–2582; (*d*) M. Hartmann, S. Kunz, D. Himsl and O. Tangermann, *Langmuir*, 2008, **24**, 8634–8642.
3 S. Kappaun, C. Slugovc and E. J. W. List, *Int. J. Mol. Sci.*, 2008, **9**, 1527–1547.
4 (*a*) M. A. Baldo, S. Lamansky, P. E. Burrows, M. E. Thompson and S. R. Forrest, *Appl. Phys. Lett.*, 1999, **75**, 4–6; (*b*) D. F. O'Brien, M. A. Baldo, M. E. Thompson and S. R. Forrest, *Appl. Phys. Lett.*, 1999, **74**(3), 442–444.
5 A. S. Rad, A. Mirabi, E. Binaian and H. Tayebi, *Int. J. Electrochem. Sci.*, 2011, **6**, 3671–3683.
6 S. Wild, G. Roglic, A. Green, R. Sicree and H. King, *Diabetes Care*, 2004, **27**, 1047–1053.
7 (*a*) D. C. Klonoff, *J. Diabetes Sci. Technol.*, 2012, **6**, 1242–1250; (*b*) B. Hu, L.-P. Zhang, M.-L. Chen and J.-H. Wang, *Biosens. Bioelectron.*, 2012, **32**, 82–88; (*c*) S. Çubuk, E. K. Yetimoğlu, M. V. Kahraman, P. Demirbilek and M. Fırlak, *Sens. Actuators, B*, 2013, **181**, 187–193; (*d*) J. C. Pickup, F. Hussain, N. D. Evans, O. J. Rolinski and D. J. S. Birch, *Biosens. Bioelectron.*, 2005, **20**, 2555–2565; (*e*) F. Khan, T. E. Saxl and J. C. Pickup, *Anal. Biochem.*, 2010, **399**, 39–43.
8 X. Yang, Z. Zhou, D. Xiao and M. M. F. Choi, *Biosens. Bioelectron.*, 2006, **21**, 1613–1620.
9 M.-L. Ho, Y.-A. Chen, T.-C. Chen, P.-J. Chang, Y.-P. Yu, K.-Y. Cheng, C.-H. Shih, G.-H. Lee and H.-S. Sheu, *Dalton Trans.*, 2012, **41**, 2592–2600.
10 M. Schlesinger, S. Schulze, M. Hietschold and M. Mehring, *Microporous Mesoporous Mater.*, 2010, **132**, 121–127.
11 N. Jung, E. Lee, J. Kim, H. Park, K.-M. Park and Y. Kang, *Bull. Korean Chem. Soc.*, 2012, **33**, 183–188.
12 B.-H. Han, I. Manners and M. A. Winnik, *Chem. Mater.*, 2005, **17**, 3160–3171.
13 L. Huynh, Z. Wang, J. Yang, V. Stoeva, A. Lough, I. Manners and M. A. Winnik, *Chem. Mater.*, 2005, **17**, 4765–4773.
14 C. S. Burke, O. McGaughey, J.-M. Sabattié, H. Barry, A. K. McEvoy, C. McDonagh and B. D. MacCraith, *Analyst*, 2005, **130**, 41–45.
15 E. O. Odebunmi and S. O. Owalude, *J. Appl. Sci. Environ. Manage.*, 2007, **11**, 95–100.
16 (*a*) Z. Yang, H. Suzuki, S. Sasaki, S. McNiven and I. Karube, *Sens. Actuators, B*, 1997, **45**, 217–222; (*b*) G. Chang, K. Morigaki, Y. Tatsu, T. Hikawa, T. Goto and H. Imashi, *Anal. Chem.*, 2011, **83**, 2956–2963.
17 G. Chang, Y. Tatsu, T. Goto, H. Imaishi and K. Morigaki, *Talanta*, 2010, **83**, 61–65.
18 X.-D. Wang, T.-Y. Zhou, X. Chen, K.-Y. Wong and X.-R. Wang, *Sens. Actuators, B*, 2008, **129**, 866–873.
19 D. Odaci, B. N. Gacal, B. Gacal, S. Timur and Y. Yagci, *Biomacromolecules*, 2009, **10**, 2928–2934.
20 Z. Zhou, L. Qiao, P. Zhang, D. Xiao and M. M. F. Choi, *Anal. Bioanal. Chem.*, 2005, **383**, 673–679.
21 (*a*) X. J. Wu and M. M. F. Choi, *Anal. Chim. Acta*, 2004, **514**, 219–226; (*b*) S. M. Borisov and O. S. Wolfbeis, *Chem. Rev.*, 2008, **108**, 423–461.
22 M.-S. Steiner, A. Duerkop and O. S. Wolfbeis, *Chem. Soc. Rev.*, 2011, **40**, 4805–4829.
23 H. Endo, Y. Yonemori, K. Musiya, M. Maita, T. Shibuya, H. Ren, T. Hayashi and K. Mitsubayashi, *Anal. Chim. Acta*, 2006, **573**, 117–124.
24 L. M. Rossi, A. D. Quach and Z. Rosenzweig, *Anal. Bioanal. Chem.*, 2004, **380**, 606–613.
25 L. Liu, N. Xia, J. Du, Q. He, Y. Qin, H. Li and C. Li, *Int. J. Electrochem. Sci.*, 2013, **8**, 9163–9170.
26 M. M. F. Choi, W. S. H. Pang, D. Xiao and X. Wu, *Analyst*, 2001, **126**, 1558–1563.

27 G. Wohlfahrt, S. Witt, J. Hendle, D. Schomburg, H. M. Kalisz and H. J. Hecht, *Acta Crystallogr., Sect. D: Biol. Crystallogr.*, 1999, **55**, 969–977.
28 T. T. K. Chi, U. T. D. Thuy, N. Q. Liem, M. H. Nam and D. Xu, *J. Korean Phys. Soc.*, 2008, **52**, 1510–1513.
29 G. Xue, Y. Guo, T. Yu, J. Guan, X. Yu, J. Zhang, J. Liu and Z. Zou, *Int. J. Electrochem. Sci.*, 2012, **7**, 1496–1511.
30 N. Fogh-Andersen and P. D'Orazio, *Clin. Chem.*, 1998, **44**, 655–659.
31 S. I. Cha, Y. Kim, K. H. Hwang, Y.-J. Shin, S. H. Seo and D. Y. Lee, *Energy Environ. Sci.*, 2012, **5**, 6071–6075.
32 A. P. Hammersley, S. O. Svensson, M. Hanfland, A. N. Fitch and D. Häusermann, *High Pressure Res.*, 1996, **14**, 235–248.
33 H. J. Kim, Y. C. Jeong, J. Heo, J. I. Rhee and K.-J. Hwang, *Bull. Korean Chem. Soc.*, 2009, **30**, 539–540.
34 C.-S. Chu, Y.-L. Lo and T.-W. Sung, *Talanta*, 2010, **82**, 1044–1051.